Geophysical Journal International

Geophys. J. Int. (2021) **226,** 524–535
Advance Access publication 2021 March 19
GJI Seismology

doi: 10.1093/gji/ggab106

The influence of fluids in the unusually high-rate seismicity in the Ometepec segment of the Mexican subduction zone

D. Legrand,[1] A. Iglesias,[2] S.K. Singh,[2] V. Cruz-Atienza,[2] C. Yoon,[3,*] L.A. Dominguez,[4] R.W. Valenzuela,[2] G. Suárez[2] and O. Castro-Artola[5]

[1]*Department Unidad Michoacan, Universidad Nacional Autónoma de México, Unidad Michoacán, Morelia,* 58190, *Mexico* .
E-mail: denis@geofisica.unam.mx
[2]*Departamento de Sismología, Universidad Nacional Autónoma de México, Mexico City,* 04510, *Mexico*
[3]*Department of Geophysics, Stanford University, Stanford, CA* 94305-2215, *USA*
[4]*Escuela Nacional de Estudios Superiores, Universidad Nacional Autónoma de México, Morelia,* 58190, *Mexico*
[5]*Department Centro de Monitoreo Vulcanológico y Sismológico, Universidad de Ciencias y Artes, Tuxtla Gutiérrez, Chiapas,* 29000, *Mexico*

Accepted 2021 March 16. Received 2021 February 8; in original form 2020 May 12

SUMMARY

The rate of earthquakes with magnitudes $M_w \leq 7.5$ in the Ometepec segment of the Mexican subduction zone is relatively high as compared to the neighbouring regions of Oaxaca and Guerrero. Although the reason is not well understood, it has been reported that these earthquakes give rise to a large number of aftershocks. Our study of the aftershock sequence of the 2012 M_w7.4 Ometepec thrust earthquake suggests that it is most likely due to two dominant factors: (1) the presence of an anomalously high quantity of overpressured fluids near the plate interface and (2) the roughness of the plate interface. More than 5400 aftershocks were manually detected during the first 10 d following the 2012 earthquake. Locations were obtained for 2419 events (with duration magnitudes $M_d \geq 1.5$). This is clearly an unusually high number of aftershocks for an earthquake of this magnitude. Furthermore, we generated a more complete catalogue, using an unsupervised fingerprint technique, to detect more smaller events (15 593 within 1 month following the main shock). For this catalogue, a high *b*-value of 1.50 ± 0.10 suggests the presence of fluid release during the aftershock sequence. A low *p*-value (0.37 ± 0.12) of the Omori law reveals a slow decaying aftershock sequence. The temporal distribution of aftershocks shows peaks of activity with two dominant periods of 12 and 24 hr that correlate with the Earth tides. To explain these observations, we suggest that the 2012 aftershock sequence is associated with the presence of overpressured fluids and/or a heterogeneous and irregular plate interface related to the subduction of the neighbouring seamounts. High fluid content has independently been inferred by magnetotelluric surveys and deduced from heat-flow measurements in the region. The presence of fluids in the region has also been proposed to explain the occurrence of slow-slip events, low-frequency earthquakes and tectonic tremors.

Key words: North America; Body waves; Earthquake source observations; Seismicity and tectonics; Dynamics: seismotectonics; Subduction zone processes.

1 INTRODUCTION

It is well known that fluids at the plate interface are a major factor in controlling the productivity of a fault system (Brodsky & Kanamori 2001; Ma *et al.* 2003; Reches & Lockner 2010). While in some cases fluids induce small earthquakes (e.g. Bachmann *et al.* 2012; Spada *et al.* 2013), in other cases fluids produce larger ruptures that otherwise will be limited by friction on the surrounding areas (Ishikawa *et al.* 2008; Hamada *et al.* 2011). In this regard, the Ometepec region is a natural laboratory with a long history of geophysical studies (e.g. Moore & Shipley 1988; Yamamoto *et al.* 2013; Husker *et al.* 2018) that exhibits dramatic effects influenced by pressurized fluids in both small and large earthquakes.

Earthquakes with magnitudes $M_w \leq 7.5$ in the Ometepec region are more frequent than in the adjacent regions of Oaxaca and Guerrero (González-Ruiz & McNally 1988; Figs 1a and b). For instance,

* Now at: Earthquake Science Center, U.S. Geological Survey, Pasadena, CA 91106, USA

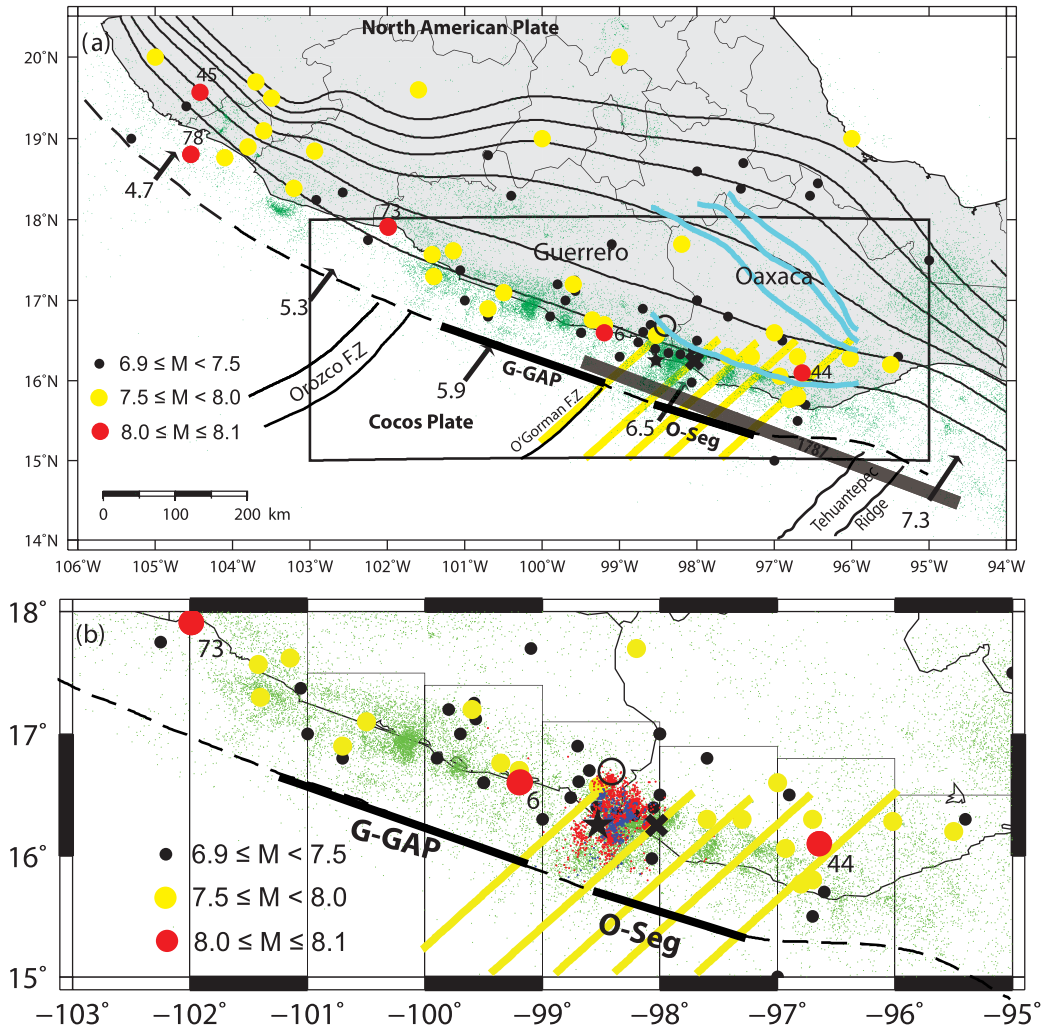

b-value	-	1.44	1.51	1.64	1.80	1.52	1.48	1.53
M<5.0	218	2222	4043	2718	7432	2757	1697	1270
5.0≤M<6.9	3	23	22	10	48	10	14	12
6.9≤M<7.5	1	2	1	8	13	2	3	1
7.5≤M<8.0	0	3	2	4	1	3	5	1
8.0≤M	0	1	0	1	0	0	1	0

Figure 1. (a) Earthquake epicentres located by the Servicio Sismológico Nacional (SSN) of Mexico between 1998 and 2015 with magnitudes less than 6.9 (green dots) and with magnitudes ≥ 6.9 (black, yellow and red dots) from 1806 to 2015, which are also listed in Table 1. Black star is the 2012 M_w7.4 Ometepec earthquake and black cross is the 2018 M_w7.2 Ometepec earthquake. Black open circle is Ometepec city. Black solid lines are the isodepth contours (from 20 to 120 km, at 20 km spacing) of the Cocos plate defined by Pardo & Suárez (1995). Blue lines are the updated isodepth contours (from 20 to 80 km, at 20 km spacing) by Fasola *et al.* (2016). Yellow lines represent seamounts from Kanjorski (2003) and UNAM Seismology-Group (2013). The spatial extent of the 1787 M_w 8.6 earthquake is shown as a grey line (Suárez & Albini 2009), and the Guerrero (G-GAP) and Oaxaca Segment (O-Seg) gaps are shown as black lines. Black rectangular inset is shown in panel (b). (b) Zoom of panel (a), with same legends. Aftershock sequence of the 2012 Ometepec earthquake located in this study: the first 30 hr (blue dots) and the eight following days (red dots). Bottom: number of earthquakes between 1998 and 2015 in windows of 1° width of longitude and bounded by the boxes in latitude. Aftershocks were not declustered from the catalogue in order to appreciate them in the counting. The total number of earthquakes in the window between 99° and 98° W (i.e. 7494) includes the aftershocks of the 2012 March 20 (M_w7.4) main shock recorded by the SSN and that from 101° and 100° W (4068) includes the much smaller aftershock sequence of the 2014 April 18 (M_w7.2) earthquake. The *b*-value for each window is calculated for the corresponding seismicity. Note that the b-value calculated here was computed using the magnitudes estimated by the SSN, rather than from the magnitudes calculated in our study, leading to different *b*-values. The relative *b*-values from one region to another can, in contrast, be compared.

since 1928, ten earthquakes with magnitude between 6.9 and 7.5 occurred in 1928, 1937, 1950, 1982 (x2), 1995, 1996, 1997, 2012 and 2018. This study focuses on the M_w7.4 Ometepec earthquake of 2012 March 20 ($18^h02'$ UTC) (Figs 1a and b) and its aftershocks. This event is a typical shallow subduction earthquake with a thrust mechanism (strike = 296°, dip = 10°, rake = 95°, depth = 20 km), compatible with the tectonics of the region. The point of nucleation was located at about 5 km offshore (UNAM Seismology Group 2013) (Fig. 1a), near the doublet rupture zone of the 1982 Ometepec earthquake (Astiz & Kanamori 1984). Previous earthquakes in this region are well described in UNAM Seismology Group (2013) and summarized in Figs 1(a) and (b), and Table 1.

The rate of occurrence of earthquakes is unevenly distributed along the contact between the Cocos and North American plates. It

Table 1. List of large earthquakes ($M_w \geq 6.9$) in Mexico from 1806 to 2015.

	Date	Latitude (°N)	Longitude (°W)	Depth (km)	*M*
1	1806/03/25	18.9	103.8		7.5
2	1818/05/31	19.1	103.6		7.7
3	1820/05/04	17.2	99.6		7.6
4	1837/11/22	20.0	105.0		7.7
5	1845/03/09	16.6	97.0		7.5
6	1845/04/07	16.6	99.2		8.1
7	1854/05/05	16.3	97.6		7.7
8	1858/06/19	19.6	101.6		7.5
9	1864/10/03	18.7	97.4		7.3
10	1870/05/11	15.8	96.7		7.9
11	1872/03/27	15.7	96.6		7.4
12	1874/03/16	17.7	99.1		7.3
13	1875/02/11	21.0	103.8		7.5
14	1875/03/09	19.4	104.6		7.4
15	1879/05/17	18.6	98.0		7.0
16	1882/07/19	17.7	98.2		7.5
17	1887/05/29	17.2	99.8		7.2
18	1889/09/06	17.0	99.7		7.0
19	1890/12/02	16.7	98.6	S	7.2
20	1894/11/02	16.5	98.0		7.4
21	1897/06/05	16.3	95.4		7.4
22	1899/01/24	17.1	100.5		7.9
23	1900/01/20	20.0	105.0		7.4
24	1900/05/16	20.0	105.0		6.9
25	1903/01/14	15.0	93.0		7.7
26	1907/04/15	16.7	99.2		7.7
27	1908/03/26	16.7	99.2		7.6
28	1908/03/27	17.0	101		7.0
29	1909/07/30	16.8	99.9		7.3
30	1909/07/31	16.6	99.5		6.9
31	1911/06/07	19.7	103.7		7.9
32	1911/12/16	16.9	100.7		7.6
33	1912/11/19	19.9	99.8		6.8
34	1913/01/15	19.0	100.0		7.5
35	1913/06/14	20.0	99.0		7.5
36	1914/03/30	19.0	96.0		7.5
37	1916/06/02	17.5	95.0		7.0
38	1917/12/29	15	97		6.9
39	1928/03/22	16.2	95.5		7.5
40	1928/06/17	16.3	96.70		7.8
41	1928/08/04	16.8	97.6		7.4
42	1928/10/09	16.3	97.3		7.6
43	1929/08/17	16.3	99.0		7.0
44	1931/01/15	16.10	96.64		8.0
45	1932/06/03	19.57	104.42	16	8.1
46	1932/06/18	19.50	103.50	13	7.8
47	1934/11/30	19.0	105.31		7.0
48	1937/07/26	18.45	96.44		7.3
49	1937/12/23	16.573	98.525	18	7.5
50	1941/04/15	18.85	102.94	s	7.7
51	1943/02/22	17.62	101.15	16	7.5
52	1946/05/15	15.5	96.7		7.0
53	1947/10/03	18.8	100.7		7.0
54	1948/01/06	17.0	98.0		6.9
55	1948/01/06	17.0	98.0		7.0
56	1950/11/17	16.8	100.7		7.0
57	1950/12/14	16.608	98.694	18	7.3
58	1951/12/12	16.5	96.9		7.0
59	1951/12/28	16.9	98.7		7.0
60	1957/07/28	16.762	99.354	18	7.5
61	1962/05/11	17.25	99.58	40	7.0
62	1962/05/19	17.12	99.57	33	7.2
63	1964/07/06	18.3	100.4		7.2
64	1965/08/23	16.024	95.928	24.7	7.8
65	1968/08/02	16.39	98.056	16	7.4

Table 1. Continued

	Date	Latitude (°N)	Longitude (°W)	Depth (km)	*M*
66	1973/01/30	18.39	103.21	32	7.5
67	1973/08/28	18.3	96.54	84	7.3
68	1978/11/29	15.77	96.80	18	7.8
69	1979/03/14	17.3	101.4	20	7.6
70	1981/10/25	17.75	102.25	20	7.3
71	1982/06/07	16.35	98.368	15	6.9
72	1982/06/07	16.40	98.538	20	7.0
73	1985/09/19	17.91	101.99	17.0	8.1
74	1985/09/21	17.57	101.42	22.0	7.6
75	1986/04/30	18.25	102.92	20.7	7.0
76	1989/04/25	16.60	99.50	19	6.9
77	1995/09/14	16.48	98.76	16	7.3
78	1995/10/09	18.81	104.54		8.0
79	1996/02/25	15.98	98.07	21	7.1
80	1997/01/11	18.34	102.58	34	7.1
81	1997/07/19	16.33	98.216	33	6.9
82	1999/06/15	18.39	97.436	70	7
83	1999/09/30	16.06	96.931		7.5
84	2003/01/22	18.77	104.104		7.6
85	2012/03/20	16.25	98.531	20	7.4
86	2014/04/18	17.38	101.055	15	7.2

increases from NW to SE, as does the convergence plate velocity (from 5.3 to 7.3 cm yr^{-1}), and the age of the subducted slab (from 7 to 23 Ma; McNally & Minster 1981; Burbach *et al.* 1984). The number of aftershocks of large earthquakes ($M_w \geq 7.0$) also increases from NW to SE (Singh & Suárez 1988; UNAM Seismology Group 2013). Surprisingly, the magnitude of instrumentally recorded earthquakes is larger to the NW part of the subduction zone relative to the SE (Klitgord & Mammerickx 1982; Singh & Suárez 1988; Anderson *et al.* 1989; Singh & Mortera 1991; Kostoglodov & Ponce 1994; Kostoglodov *et al.* 1996; UNAM Seismology Group 2013; Fig. 1a). The small number of large earthquakes recorded in the SE part of the subduction may be the result of the short-time window of observation. However, it has also been interpreted as a result of the low coupling of the plate in the SE part of the subduction zone (Kostoglodov & Ponce 1994). Hence, the origin of the high-rate seismicity of aftershocks of large earthquakes in the SE subduction segment is not well understood. In this paper, we aim to better understand the reason for the unusually high seismic activity in the Ometepec region, in particular through the magnitude and temporal distributions of the 2012 M_w7.4 Ometepec aftershock sequence.

2 DATA AND METHODS

The M_w7.4 main shock of 20 March 2012 was recorded by almost 40 permanent accelerometers and broad-band regional seismometers (four of them at a distance less than 200 km) belonging to the Servicio Sismológico Nacional (SSN). Eight additional local accelerometers (at distances less than 70 km) belonging to UNAM's Instituto de Ingeniería and CIRES (Centro de Instrumentación y Registro Sísmico) recorded the earthquake. The closest seismic/geodetic station, PNIG, is located at a distance of ∼46 km Northeast of the main-shock epicentre (Fig. 2). Instrumentation at this station includes of a three-component broad-band seismometer (which stopped recording ∼6.5 s after the main shock, that is, 0.5 s after the arrival of the *S*-wave, and during the following 4 hr due to a power outage), an accelerometer and a GPS receiver (sampled at 1 Hz). Some of these records are shown in UNAM Seismology Group (2013).

30 hr after the main shock, a portable seismic network consisting of six broad-band seismometers was deployed mainly to the northeast of the main shock (Oaxaca State) (Green inverted triangles in Fig. 2). Only two stations were installed in Guerrero State close to the Oaxaca-Guerrero border due to security reasons. Data from the portable network is available from 22 March (00^h00 UTC) through 29 March (16^h00 UTC) 2012. Hence, a total of seven local, broad-band seismometers, including permanent station PNIG (Fig. 2), are used here to locate the aftershock sequence composed of 10 days of data (days 20 and 21 March using PNIG station and days 22 to 29 using PNIG and the portable seismic network). All times in this study are in UTC, except Suporting Information Fig. S4.

The aftershock sequence of the 2012 Ometepec earthquake was analysed as follows: (1) The main shock was located using two methods. The first method used arrival times of *P* and *S* waves recorded on the regional seismic stations, while the second one used the polarization direction of the *P* wave in the closest station (PNIG) as well as the distance deduced from the *S*—*P* arrival times to that station (Figs 1b and 2). (2) 453 aftershocks during the first 30 hr were detected manually and located using the single, three-component permanent station PNIG (Fig. 2). (3) 1966 aftershocks that occurred after the first 30 hr (until 29 March) were also detected manually when they were seen on at least 4 stations, and then located using arrival times of *P* and *S* waves of a local, portable seismic network deployed by the Institutes of Geophysics and Engineering at Universidad Nacional Autónoma de México (UNAM) one and a half day after the main shock, in addition to data from station PNIG using the second method (Fig. 2). (4) The *P*- and *S*-wave velocity ratio V_p/V_s∼1.70 was determined from picks of *P* and *S* arrival times (generalized Wadati method, see the Suporting Information) and used to locate the aftershocks. (5) The location errors of the first 30 hr of aftershocks using only the PNIG station were estimated by comparison to common earthquakes recorded by the portable seismic network. (6) The fault dimension of the main shock was estimated using the spatial distribution of aftershocks, and then compared with empirical scaling relations between magnitude and size of earthquakes. (7) The size and location of the 2012 aftershock sequence was compared to the 1982 sequence. All the details of this

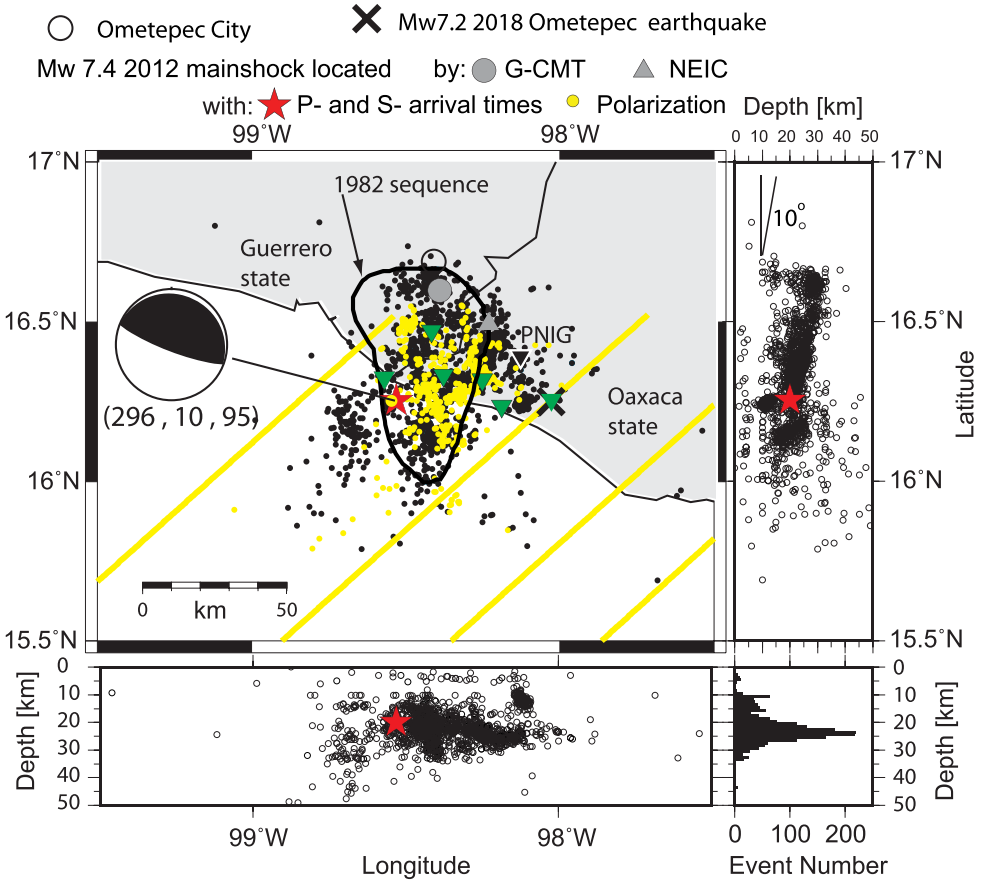

Figure 2. Earthquake locations for the two following data sets: (1) the epicentres of the earthquakes of the first 30 hr following the main shock are shown as yellow dots only in the horizontal plane because the depths were fixed. These 453 events were located using the single broad-band seismometer PNIG (black inverted triangle); (2) the second set of 1966 aftershocks are shown as black dots and were located using the *P* and *S* arrival times of four to seven stations (green inverted triangle and the black inverted triangle) from 2012 22 March 22 through March 29. The epicentre of the M_w7.4, 2012 Ometepec earthquake located by the US NEIC (National Earthquake Information Center; grey triangle, https://earthquake.usgs.gov/earthquakes/search/), Global Centroid Moment Tensor (G-CMT) project (grey circle, https://www.globalcmt.org/CMTsearch.html), with local and regional Mexican network (red star, which is the preferred location), and with the polarization method (yellow circle inside the red star) using the single permanent PNIG station. The black contour bounds the aftershocks of the two 1982 earthquakes. The black cross is the M_w7.2, 2018 earthquake. Green inverted triangles represent the local, temporary seismic network. Seamount chains are represented by the yellow lines. The angle of 10° in the top right figure shows the trend of the largest aftershocks, compatible with the dip of the focal mechanism of the main shock. The focal mechanism of the main shock is plotted with its associated (strike, dip, rake) values. The depth slices are north–south (right) and west–east (bottom).

process are described in the Suporting Information. (8) An additional earthquake catalogue was automatically computed, starting just after the main shock until 20 April (31 d in total). We applied fingerprint waveform analysis (Yoon *et al.* 2015) to detect small events in the aftershock sequence, in order to precisely examine the Gutenberg–Richter and Omori laws, and tidal effects on the seismicity rate. We checked that the number of earthquakes per hour is not affected by reduced anthropogenic activity at night, relative to during the day. This is mainly due to the fact that the PNIG station is a very isolated station, at about 10 km NW of Pinotepa Nacional, the closest village, which is a very small (about 30 000 habitants in 2010), with little industrial activity (Suporting Information Fig. S4).

Here, we describe the computation of an automatic detector based on Big Data analysis. Advances in data intensive computing techniques allow standardized search for similar signals in large continuous data sets, which would otherwise be impractical with standard methods. Some examples of applications include: detection of nearly identical websites and documents to identify plagiarism, and music identification of similar audio clips. Yoon *et al.*(2015) developed a search algorithm based on unsupervised machine learning techniques named fingerprint and similarity thresholding (FAST). This method examines the entire continuous seismic record in search of similar earthquake-like signals. Unlike traditional methods for earthquake detection, fingerprint analysis does not require templates or *a priori* information about the nature of the earthquakes as input signals, but provide comparable detection performance as template matching (Yoon *et al.* 2017). Use of benchmark problems demonstrated that this algorithm provides high detection sensitivity, computational efficiency, and general applicability (Yoon *et al.* 2015).

We performed an automatic search for previously unknown small earthquakes using FAST algorithm at the closest three-component station (PNIG) to the epicentral location of the M_w 7.4 2012 Ometepec earthquake. FAST detected 15 593 aftershocks from the time of the M_w 7.4 main shock until 31 d after (2012 April 20). 90 per cent of these aftershocks occurred within 52 km from the PNIG station, according to the *S*–*P* time. 1047 detections were removed from the

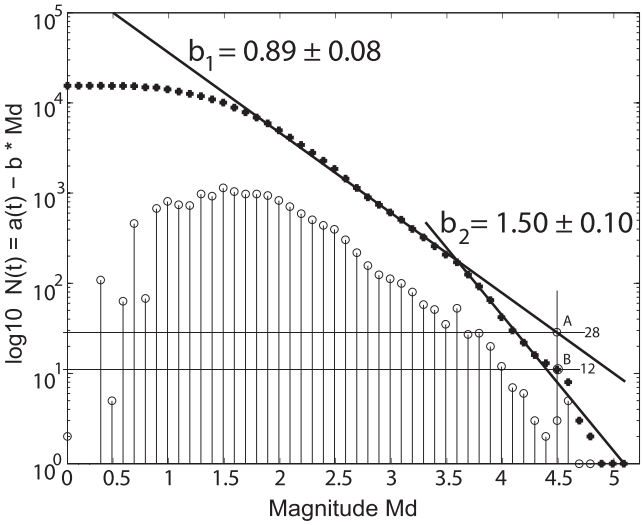

Figure 3. The earthquake-magnitude distribution of the 15 593 aftershocks (including the first 30 hr just after the main shock detected with the PNIG station). $N(t)$ is the number of earthquakes of duration magnitude $\geq M_d$ for 31 d. The cumulative distribution is shown as closed diamonds and the non-cumulative distribution as vertical lines with top open circles.

original detection set after visual inspection, which we consider as false detections. In contrast, only 439 earthquakes were reported by the SSN within 52 km radius from the PNIG station during the same time period. Many more small magnitude earthquakes can therefore be associated with the post-seismic processes induced by the main shock.

3 RESULTS

3.1 The earthquake magnitude–frequency distribution and Omori scaling law

The local duration-magnitude, M_d, was calculated for the aftershocks (Lee *et al.* 1972). The *b*-value of the Gutenberg-Richter (GR) law was calculated for the automatic detection catalogue with 15 593 aftershocks (i.e. including the earthquake magnitudes of the first 30 hr just after the main shock), using the maximum likelihood method (Aki 1965). Fig. 3 shows both, the cumulative (in closed diamonds) and non-cumulative (in vertical lines with top open circles) plots for the magnitude–frequency distribution of earthquakes. We have a *b*-value of 0.89 ± 0.08 for magnitudes between 1.8 and 3.6.

The corresponding Omori law corrected for completeness is shown in Fig. 4(a). A *p*-value of 0.37 ± 0.12 was found, which indicates a slowly decaying aftershock sequence. The date of the main shock (2012 March 20 is plotted as a white circle in Fig. 4a) was not taken into account in the calculation of the *p*-value because the main shock occurred at the end of the day, so few aftershocks were recorded during that day. The resulting *p*-value is very low. In order to confirm this low *p*-value, we calculated it with the SSN catalogue until the end of May, where we found a similarly low *p*-value of 0.56 ± 0.02 (Fig. 4b). We will consider the 0.37 *p*-value as more reliable because of the better completeness of the catalogue with respect to the SSN one.

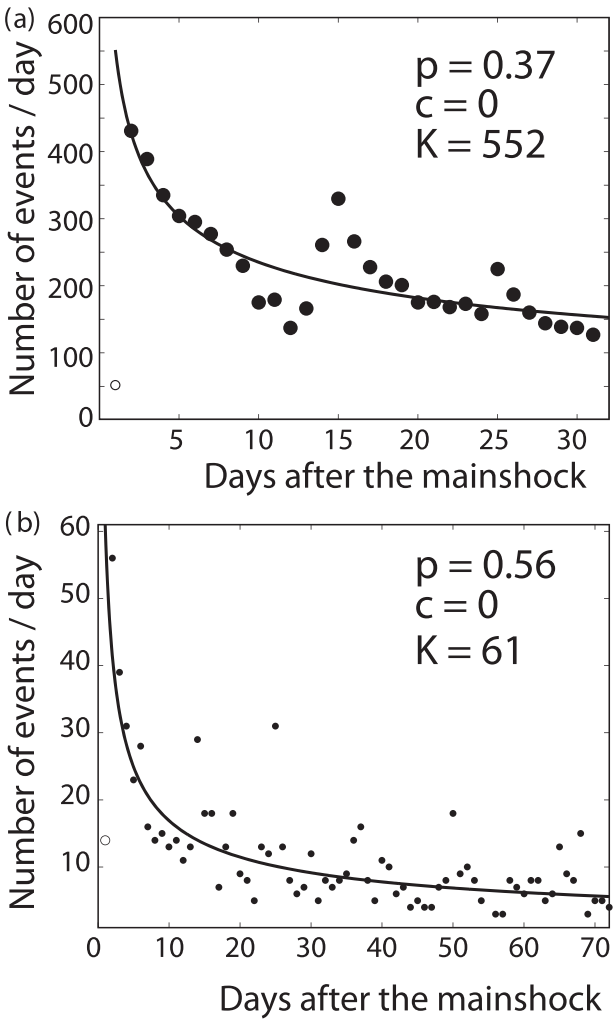

Figure 4. (a) Daily number of aftershocks corrected for completeness of the first 31 d (black circles) as function of time and the fit (solid black line) to the Omori law $dN(t)/dt = K/(t+c)^p$. The day when the main shock occurred is plotted as a white circle and is not taken into account in the calculation of *p*-value because the main shock occurred at the end of the day and few aftershocks were recorded that day. The black circles are taken into account in the calculation of the *p*-value. (b) Same with the data of the SSN, until end of May.

3.2 Time evolution of seismicity

Periodicity in the timing of earthquakes was computed using a statistical approach through the application of the Schuster test (Ader & Avouac 2013) on the automatic aftershock detections obtained using fingerprint analysis described in section 3.1. The significance of a given period can be computed by comparison of the probability of the event occurring randomly against the probability of the event occurring as a result of a modulated seismic rate (Cochran *et al.* 2004; Thomas *et al.* 2009; Ader & Avouac 2013; Dutilleul *et al.* 2015). Fig. 5 shows the modified Schuster test (i.e. Schuster spectrum), where we show the existence of two dominant periods at 12.54 and 24.49 hr (red circles), which clearly exceed the probability expected from a random distribution. The Schuster test suggests a strong correlation between the earthquake occurrence and the occurrence of the strongest Earth tides. Using the numerical software TSoft (Van Camp & Vauterin 2005), we estimated the dominant periods of the synthetic tide calculated at the hypocentre starting

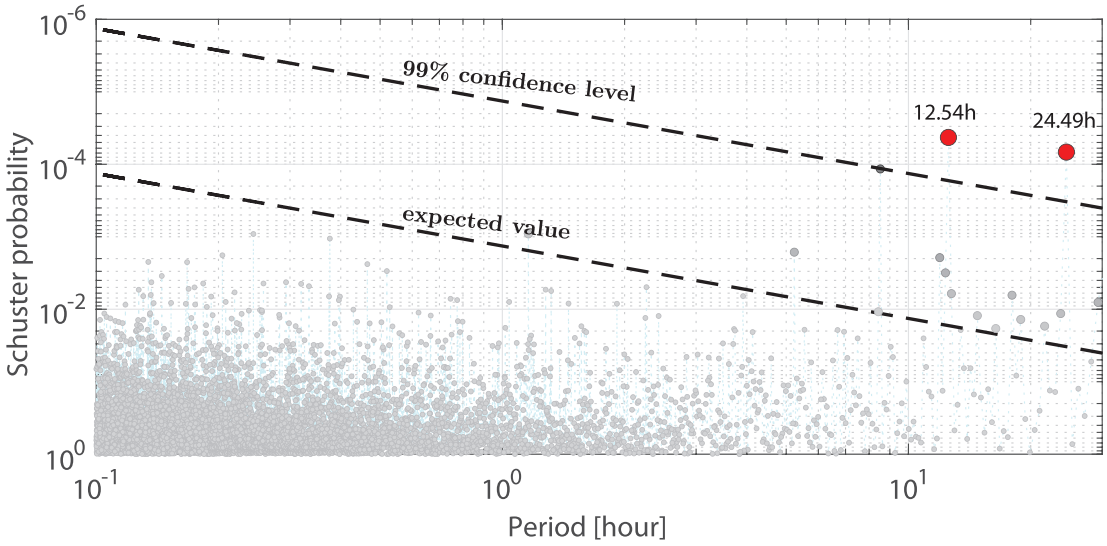

Figure 5. Schuster spectrum over the automatic aftershock catalogue of length 31 d, between periods $T_{min} = 10^{-1}$ hr and $T_{max} = 30$ hr. Two main periods of ∼12.5 and ∼24.5 hr are present in the earthquake catalogue.

at the time of the event which revealed two dominant periods for the diurnal tide of 12.3 and 24–25 hr, that are consistent with the estimates from the Schuster spectrum.

4. DISCUSSION

4.1 Regional seismicity

The Ometepec region (-99° W < longitude ≤ -98° W, 15° N ≤ latitude ≤ 17° N) has a higher rate of seismic activity (13 earthquakes of magnitudes $6.9 \leq M_w < 7.5$ between 1806 and 2015) relative to the rest of the Mexican subduction zone (e.g. Yamamoto *et al.* 2013; Figs 1a and b) and a remarkably high number of smaller events with magnitudes below 5.0 (Fig. 1b). The presence of this zone of high seismic activity coincides with a denser region of seamounts approaching the trench (Kanjorski 2003; UNAM Seismology Group 2013), inducing a rougher contact at the plate interface.

4.2 Presence of water and heterogeneous medium

4.2.1 High b-value of the earthquake-magnitude distribution

The *b*-value (b = 0.89 ± 0.08) of the 2012 Ometepec aftershock sequence (Fig. 3) for magnitudes between 1.8 and 3.6 is expected for a 'typical' tectonic earthquakes for which $b \leq 1$ (Gutenberg & Richter 1949, 1954; Lay & Wallace 1995). The magnitude of completeness of 1.8 was achieved thanks to the automatic search for previously unknown small earthquakes using FAST algorithm at the closest three-component station (PNIG). Nevertheless, we can observe a much higher b-value of 1.5 ± 0.1 for magnitudes greater than 3.6 which is unusually high for a unique tectonic origin. A change in the slope of the earthquake-magnitude distribution generating two b-values has been observed in many cases when fluids (water and/or magma) are present, as on volcanoes (Filson *et al.* 1973; Francis 1974; Caplan-Auerbach & Duennebier 2001; Legrand *et al.* 2004, 2015; Neunhöfer & Hemmann 2005; Kundu *et al.* 2012) or in tectonic contexts like Taiwan (Wang 1988) and the San Andreas fault (Vorobieva *et al.* 2016). We want to understand why large magnitude ($M_d > 3.6$) events do not fit properly within a general Gutenberg–Richter distribution. We can interpret the earthquake-magnitude distribution in three different ways: (i) the presence of a unique linear slope between magnitudes 1.8 and 3.6, with a *b*-value $b_1 = 0.89 \pm 0.08$; (ii) the presence of a unique linear slope between magnitudes 3.6 and 5.2, with a *b*-value $b_2 = 1.50 \pm 0.10$; (iii) the presence of two slopes: the first with magnitudes between 1.8 and 3.6 and the second one between 3.6 and 5.2.

In the first interpretation, the earthquakes with magnitudes $M_d > 3.6$ deviate from the linear part of the earthquake-magnitude distribution (i.e. they are in deficit with respect to the number expected with the slope $b_1 = 0.89$), and could correspond, in theory, to an incomplete catalogue for the largest events. Nevertheless, such a case is unlikely since PNIG station is sufficiently close from the hypocentres ensuring the detection of all the events of magnitude greater than 3.6. For instance, if the slope of 0.89 is considered valid for magnitudes > 3.6, we should have recorded 28 earthquakes of magnitudes greater than 4.5 (point A on Fig. 3), however only 12 earthquakes with magnitude greater or equal to 4.5 were recorded (point B on Fig. 3). Neither our catalogue nor the SSN catalogue reports any of these missing events. Furthermore, the largest aftershock does not follow Bath law which indicates that the difference between the main shock and the largest aftershock magnitude is 1.2 regardless of the magnitude of the main shock (Helmstetter & Sornette 2003). In our case, the largest aftershock is of magnitude 5.2, 2.2 below the main shock one. Hence, we have a deficit of large earthquakes (with magnitudes greater than 3.6) thus a second slope is needed for these magnitudes.

The second interpretation corresponds to a unique linear slope for the largest magnitudes (between 3.6 and 5.2). This interpretation is plausible because the earthquake catalogue for large magnitudes is complete. The corresponding b-value for this range of values is $b_2 = 1.50 \pm 0.10$ (Fig. 3). Therefore, an issue is to know what magnitude, among the $M_{c1} = 1.8$ and $M_{c2} = 3.6$, is the magnitude of completeness of the whole catalogue (i.e. if the break of the earthquake-magnitude distribution is real or artificial). Moreover, the number of events recorded during the day and the night periods

for magnitudes greater than 1.8 is similar (see Suporting Information Fig. S4), hence the daily noise did not affect the detection of these magnitudes around 1.8. Therefore, we can adopt as magnitude of completeness of the whole catalogue $M_c = 1.8$ and not 3.6. Hence, the linear part of the earthquake-magnitude distribution between 1.8 and 3.6 leads to a deficit of earthquakes of magnitude > 3.6.

If each of these segments of the earthquake-magnitude distribution is representative of different tectonic mechanisms: one fluid related and the other fault aftershock type, we consider that the earthquake-magnitude distribution of Fig. 3 can be explained by a dual manner. Therefore, the break observed at magnitude 3.6 reveals the limit between these dominant mechanisms. In conclusion, we model the earthquake-magnitude distribution using a bimodal distribution. The first one, for magnitudes between 1.8 and 3.6, $b_1 = 0.89 \pm 0.08$; and the second one, for magnitudes between 3.6 and 5.2, $b_2 = 1.50 \pm 0.10$.

The analysis of the Omori law (Fig. 4) shows that the aftershock sequence lasted two months and after the 13 of April and until 24 July (four months after the main shock), no earthquake of magnitude greater than 4.5 was recorded by the SSN. High *b*-values (from 1.2 to 2.6) are frequently observed in environment where fluids (water and/or magma) are involved in the rupture process. This is usually the case for volcano-tectonic earthquakes (Francis 1968a, 1968b, 1974; Hill 1977; McNutt 1986; Matsumura *et al.* 1991; Wiemer & Benoit 1996; Wiemer & McNutt 1997; Murru *et al.* 1999; Wyss *et al.* 2001; Del Pezzo *et al.* 2003; Legrand *et al.* 2004, 2011, 2012, 2015; Montgomery-Brown *et al.* 2009; Kundu *et al.* 2012) or for induced seismicity in geothermal fields caused by water injection (Wyss 1973; Cornet *et al.* 1997; Cuénot *et al.* 2008; Dorbath *et al.* 2009; Bachmann *et al.* 2012).

The presence of fluids promotes the generation of microcracks more easily by reducing the frictional strength on the pre-existing faults due to the lowering of the effective normal stress. As a consequence, fluids induce a higher number of small earthquakes in comparison with larger events, leading to increased *b*-values (Scholz 1968; Wyss 1973), which has been confirmed by numerical models (e.g. Henderson & Maillot 1997). A very small increase of the pore fluid pressure (<1 MPa) may be enough for such a phenomenon to occur (Hubbert & Rubey 1959; Healy *et al.* 1968; Scholz 1968; Wyss 1973; Pearson 1981; Pine & Batchelor 1984; Fehler 1989; Guha 2000). Generation of relatively large amount of small earthquakes (i.e. lack of large events) may be explained by the frequent occurrence of aseismic slip in the interface. The presence of fault zone fluids promotes slow-slip events that release a significant part of the necessary strain energy to generate large ruptures. Such aseismic slip triggered by fluid-induced pressure changes may affect larger regions than those directly conditioned by fluids (Bhattacharya & Viesca 2019).

The effect of fluids in aftershock sequences has been observed in several places. For example, a spatiotemporal analysis of aftershocks of the 2004 M_w9.2 Sumatra–Andaman earthquake indicates the presence of ascending fluids released from the subducting oceanic crust (Waldhauser *et al.* 2012). The presence of fluids in the Guerrero-Oaxaca region has been suggested due to the existence of an ultra-low velocity layer (Song *et al.* 2009; Dougherty & Clayton 2014), the occurrence of slow-slip events (e.g. Franco *et al.* 2005; Brudzinski *et al.* 2010; Radiguet *et al.* 2012; Graham *et al.* 2016; Maury *et al.* 2018), the presence of tectonic tremors (Payero *et al.* 2008; Brudzinski *et al.* 2010; Kostoglodov *et al.* 2010; Husker *et al.* 2012; Cruz-Atienza *et al.* 2015; Fasola *et al.* 2016; Skoumal *et al.* 2016; Villafuerte & Cruz-Atienza 2017) and the existence of (very) low frequency events (Frank *et al.* 2013, 2014; Maury *et al.* 2016).

Fluids have been proposed as a predominant factor in the origin of these signals worldwide (Kodaira *et al.* 2004; Shelly *et al.* 2006; Liu & Rice 2007; Segall *et al.* 2010; Peacock *et al.* 2011; Katayama *et al.* 2012). The released fluids migrate upward towards the surface, more likely along the plate interface, and are responsible of the high aftershock rate, systematically observed for moderate earthquakes (Astiz & Kanamori 1984; Beroza *et al.* 1984; Singh & Suárez 1988; Yamamoto *et al.* 2002; UNAM Seismology Group 2013; 2013), leading in some cases to high *b*-values. Kim *et al.* (2010) proposed that the upper oceanic crust is highly heterogeneous, composed of hydrous minerals (talc) that dehydrate at a depth of ∼40 km, and thus result in dewatering. Furthermore, magneto-telluric studies suggest the presence of abundant fluids, squeezed from the slab, probably along or near the subduction interface (Jödicke *et al.* 2006; Song *et al.* 2009; Husker *et al.* 2018), that may trigger the tectonic tremors (Song *et al.* 2009; Brudzinski *et al.* 2010; Husker *et al.* 2012; Villafuerte & Cruz-Atienza 2017). In the Guerrero region, to the NW of Ometepec, tectonic tremors occur where overpressured fluids exist (Kostoglodov *et al.* 2010; Husker *et al.* 2012; Villafuerte & Cruz-Atienza 2017), so that spatial variations of fluid pressure may be responsible for the observed rapid tremor migration (Cruz-Atienza *et al.* 2018). High heat flow, about 110 mW m^{-2} in the Ometepec region also favours dehydration at 40–50 km depth (Song *et al.* 2009; Manea & Manea 2011).

High *b*-values may also be the result of highly heterogeneous and fractured materials (Mogi 1962), or highly porous rocks containing many microfractures (Scholz 1968). In a heterogeneous medium due to prominent variations of the plate interface geometry, fluids can be trapped but may also migrate more easily due to stress concentrations and generation of fractures. It is then difficult to attribute high b-values to only one process. It appears that the high b-values observed in Ometepec are likely due to a combination of both effects: a heterogeneous plate interface and the presence of fluids. In the Ometepec region, such heterogeneities (geometrical irregularities) are due to the subduction of several parallel ridges (i.e. seamounts) oriented in a NE direction, roughly aligned with the slab convergence direction (Kanjorski 2003; Kim *et al.* 2010; UNAM Seismology Group 2013; Yamamoto *et al.* 2013; Fig. 2).

We conclude that the combined effect of heterogeneities and the presence of water affect the characteristics of the local seismicity, leading to a high *b*-value of the earthquake-magnitude distribution. It is not completely clear why the Ometepec region has a much higher seismicity rate than the nearby Oaxaca segment with similar characteristics. It is still an open question and additional processes may be responsible for this surprising observation.

4.2.2 An unusually low decay rate of the aftershock sequence

Typical *p*-values vary between 1.0 and 1.4 (Lay & Wallace 1995). The extremely low *p*-value (0.37 calculated for the 31-d sequence, and 0.56 for the two and a half months time window, Fig. 4) of the 2012 aftershock sequence is unusual for an M_w7.4 thrust earthquake. It is consistent with previous observations pointing out that the Ometepec region has a higher seismicity rate of large magnitudes (M_W∼7 to 7.5) with respect to other regions in Mexico (González-Ruiz & McNally 1988), along with relatively large number of aftershocks that persist for several months after a main shock (Singh & Suárez 1988; UNAM Seismology Group 2013). The low *p*-value we found is an illustration of such high-rate seismicity and

may be due also to the presence of fluids and/or the presence of heterogeneities in the plate interface and the upper crust as discussed earlier.

4.2.3 Correlation between the high rate of seismicity and Earth tides

In order to detect periodicity in the catalogue of 15 593 earthquakes, we performed a Schuster spectrum (Fig. 5) as mentioned before. Two dominant periods are extracted from these data, at ∼12.5 and ∼24.5 hr. The gravitational pull of the combined effect of the Sun and the Moon induces Earth tides at this place at that time with two periods of ∼12.3 hr (semi-diurnal) and ∼24–25 hr (diurnal) that we calculated using the software TSoft (Van Camp & Vauterin 2005). They are very similar to the dominant periods in the Ometepec earthquake catalogue. It has been shown that Solid Earth tides can temporally modulate the occurrence of crustal earthquakes in different tectonic contexts, especially in convergent margins around the Pacific (Emter 1997; Glasby & Kasahara 2001; Tanaka *et al.* 2002, 2004; Cochran *et al.* 2004; Hill & Prejean 2007). Tidal modulation of aftershock sequences (e.g. Ryall *et al.* 1968), tectonic tremor (e.g. Nakata *et al.* 2008; Rubinstein *et al.* 2008; Ide & Tanaka 2014; Houston 2015; Yabe *et al.* 2015; Ide *et al.* 2016) and low-frequency earthquakes (Thomas *et al.* 2012) has also been systematically observed across the globe, including Mexico (Peng & Rubin 2017; Maury *et al.* 2018). For instance, tectonic tremor sensitivity to tidal stressing increases with pore pressure as the surrounding aseismic slip develops (Houston 2015; Peng & Rubin 2017). Tide effects on repeating seismicity, including low-frequency events, have also been suggested in the Guerrero gap (Frank *et al.* 2016). Seismic modulation by Earth tides is observed also in volcanic and geothermal areas (Klein 1976; McNutt & Beavan 1981; Sparks 1981; Tolstoy *et al.* 2002; Espíndola *et al.* 2006), where fluids such as magma and/or water are present. The tidal triggering of earthquakes is commonly explained by the presence of fluids (Lockner & Beeler 1999; Audet *et al.* 2009; Song *et al.* 2009; Thomas *et al.* 2009; Delorey *et al.* 2017). Given that this effect is much better observed on earthquakes of small magnitudes, it is often difficult to detect in common catalogs, but such observations have been documented by high-resolution studies (Tsuruoka *et al.* 1995; Cochran *et al.* 2004; Métivier *et al.* 2009; Tanaka 2010, 2012; Ide *et al.* 2016; Delorey *et al.* 2017). Even though the stress loading (0.1–10 kPa) due to Earth tides is small with respect to tectonic stresses (1–100 MPa), its rate is not (∼1 kPa hr^{-1}). The stress rate due to the Earth tides can in fact exceed the tectonic stressing rates (Sparks 1981; Emter 1997; Sottili *et al.* 2007). The presence of fluids may drastically reduce the effective normal stress in the plate interface (Peacock *et al.* 2011) making small changes in the external load, such as those induced by the Earth tides, be enough to induce small earthquakes. In our case, the presence of nearby stations allows us to detect small aftershocks and thus find their correlation with Earth tides.

5. CONCLUSION

The Ometepec region has a very specific behaviour where many small earthquakes are generated much more than largest ones in the nearby regions. The unusually high rate of seismicity observed in the Ometepec region may be due to the combination of two effects: (1) the presence of overpressured fluids at the plate interface and (2) a highly heterogeneous medium associated with the subduction of seamounts in this region. These conditions may explain the seismic observations of the 2012 Ometepec aftershock sequence: an anomalously large number of small magnitude aftershocks ($M_d \leq 3.6$) together with a deficit of large aftershocks ($M_d \geq 3.6$); the presence of a high *b*-value of the Gutenberg–Richter law; a very low *p*-value of the Omori law; and regular peaks of seismic activity every ∼12.5 and ∼24.5 hr related to the Earth tides. The presence of fluids in the Ometepec region is supported by a variety of former studies including magnetotelluric and heat-flow measurements, as well as the occurrence of tectonic tremors, slow-slip events and low-frequency earthquakes.

ACKNOWLEDGEMENTS

We thank Servicio Sismológico Nacional for the earthquake catalogue (http://www.ssn.unam.mx/). The research of DL has been partially supported by the PASPA DGAPA, UNAM programme. The FAST software for similar earthquake detection is available at https://github.com/stanford-futuredata/FAST. We would like to thank two anonymous reviewer and editor to significantly improve this work.

REFERENCES

Ader, T. & Avouac, J.P., 2013. Detecting periodicities and declustering in earthquake catalogs using the Schuster spectrum, application to Himalayan seismicity, *Earth planet. Sci. Lett.,* **377,** 97–105

Aki, K., 1965. Maximum likelihood estimate of *b* in the formula log (*N*) = a − *bM* and its confidence limits, *Bull. Earthq. Res. Inst. Univ. Tokyo,* **43,** 237–239.

Anderson, J., Singh, S., Espindola, J.M. & Yamamoto, J., 1989. Seismic strain release in the Mexican subduction thrust, *Phys. Earth planet. Inter.,* **58,** 307 –322.

Astiz, L. & Kanamori, H., 1984. An earthquake doublet in Ometepec, Guerrero, Mexico, *Phys. Earth planet. Inter.,* **34,** 24–45

Audet, P., Bostock, M., Christensen, N. & Peacock, S., 2009. Seismic evidence for overpressured subducted oceanic crust and megathrust fault sealing, *Nature,* **457,** 76 –78.

Bachmann, C., Wiemer, S., Goertz-Allmann, B. & Woessner, J., 2012. Influence of pore-pressure on the event-size distribution of induced earthquakes, *Geophys. Res. Lett.,* **39,** doi:10.1029/2012GL051480.

Beroza, G., Rial, J. & McNally, K., 1984. Source mechanism of the June 7, 1982 Ometepec, Mexico earthquake, *Geophys. Res. Lett.,* **11,** 689–692.

Bhattacharya, P. & Viesca, R.C., 2019. Fluid-induced aseismic fault slip outpaces pore-fluid migration, *Science,* **364,** 464 –468.

Brodsky, E.E. & Kanamori, H., 2001. Elastohydrodynamic lubrication of faults, *J. geophys. Res.,* **106,** 16 357–16 374.

Brudzinski, M.R., Hinojosa-Prieto, H.R., Schlanser, K.M., Cabral-Cano, E., Arciniega-Ceballos, A., Diaz-Molina, O. & DeMets, C., 2010. Nonvolcanic tremor along the Oaxaca segment of the Middle America subduction zone, *J. geophys. Res.,* **115,** doi:10.1029/2008JB006061.

Burbach, G.V., Frohlich, C., Pennington, W.D. & Matumoto, T., 1984. Seismicity and tectonics of the subducted Cocos plate, *J. geophys. Res.,* **89,** 7719 –7735

Caplan-Auerbach, J. & Duennebier, F., 2001. Seismicity and velocity structure of Loihi seamount from the 1996 earthquake swarm, *Bull. seism. Soc. Am.,* **91,** 178 –190.

Cochran, E., Vidale, J. & Tanaka, S., 2004. Earth tides can trigger shallow thrust fault earthquakes, *Science,* **306,** 1164–1166

Cornet, F.H., Helm, J., Poitrenaud, H. & Etchecopar, A., 1997. Seismic and aseismic slips induced by large-scale fluid injections, *Pure appl. Geophys.,* **150,** 563 –583.

Cruz-Atienza, V., Husker, A., Legrand, D., Caballero, E. & Kostoglodov, V., 2015. Nonvolcanic tremor locations and mechanisms in Guerrero, Mexico, from energy-based and particle motion polarization analysis, *J. geophys. Res.,* **120,** 275–289.

Cruz-Atienza, V., Villafuerte, C. & Bhat, H., 2018. Rapid tremor migration and pore-pressure waves in subduction zones, *Nat. Commun.,* **9,** 2900, doi:10.1038/s41467-018-05150-3.

Cuénot, N., Dorbath, C. & Dorbath, L., 2008. Analysis of the microseismicity induced by fluid injection in the Hot Dry Rock site of Soultzsous-Forêts (Alsace, France): implications for the characterization of the geothermal reservoir properties, *Pure appl. Geophys.,* **165,** 797–828

Delorey, A., vanderElst, N. & Johnson, P., 2017. Tidal triggering of earthquakes suggests poroelastic behavior on the San Andreas Fault, *Earth. planet. Sci. Lett.,* **460,** 164–170

Del Pezzo, E., Bianco, F. & Saccorotti, G., 2003. Duration magnitude uncertainty due to seismic noise: inference on the temporal pattern of G-R *b*-value at Mt. Vesuvius, Italy, *Bull. seism. Soc. Am.,* **93,** 1847–1857

Dorbath, L., Cuénot, N., Genter, A. & Frogneux, M., 2009. Seismic response of the fractured and faulted granite of Soultz-sous-Forêts (France) to 5 km deep massive water injections, *Geophys. J. Int.,* **177,** 653–675

Dougherty, S. & Clayton, R., 2014. Seismicity and structure in central Mexico: evidence for a possible slab tear in the South Cocos plate, *J. geophys. Res.,* **119,** 3424–3447.

Dutilleul, P., Johnson, C., Burgmann, R., Wan, Y. & Shen, Z., 2015. Multifrequential periodogram analysis of earthquake occurrence: an alternative approach to the Schuster spectrum, with two examples in central California, *J. geophys. Res.,* **120,** 8494 –8515.

Emter, D., 1997. Tidal triggering of earthquakes and volcanic events, in *Tidal Phenomena,* Lecture Notes in Earth Sciences, Vol. 66, pp. 293–309, eds. Wilhelm, H., Zurn, W. & Wenzel, H.-G., Springer.

Espíndola, J.M., Zamora-Camacho, A. & Jiménez, Z., 2006. Some aspects of the seismicity associated with the 1982 eruption of El Chichon Volcano, Chiapas, Mexico, *J. Volc. Geotherm. Res.,* **157,** 367–374

Fasola, S. *et al.*, 2016. New perspective on the transition from flat to steeper subduction in Oaxaca, Mexico based on seismicity, nonvolcanic tremor, and slow slip, *J. geophys. Res.,* **121,** 1835–1848.

Fehler, M., 1989. Stress control of seismicity pattern observed during hydraulic fracturing experiments in the Fenton Hill hot dry rock geothermal energy site, New Mexico, *Int. J. Rock Mech. Min. Sci. Geomech.,* **26,** 211–219

Filson, J., Simkin, T. & Leu, L., 1973. Seismicity of a caldera collapse: Galapagos Islands 1968, *J. geophys. Res.,* **78,** 8591 –8621.

Flinn, E., 1965. Signal analysis using rectilinearity and direction of particle motion, *Proc. IEEE,* **53**(12), 1874–1876.

Francis, T., 1968a. The detailed seismicity of mid-oceanic ridges, *Earth planet. Sci. Lett.,* **4,** 39–46.

Francis, T., 1968b. Seismicity of mid-oceanic ridges and its relation to properties of the upper mantle and crust, *Nature,* **220,** 899 –901.

Francis, T., 1974. A new interpretation of the 1968 Fernandina caldera collapse and its implications for the mid-oceanic ridges, *Geophys. J. R. astr. Soc.,* **39,** 301 –318.

Franco, S., Kostoglodov, V., Larson, K., Manea, V., Manea, M. & Santiago, J., 2005. Propagation of the 2001–2002 silent earthquake and interplate coupling in the Oaxaca subduction zone, Mexico, *Earth Planets Space,* **57,** 973–985

Frank, W., Shapiro, N., Kostoglodov, V., Husker, A., Campillo, M., Payero, J. & Prieto, G., 2013. Low-frequency earthquakes in the Mexican Sweet Spot, *Geophys. Res. Lett.,* **40,** 2661–2666.

Frank, W., Shapiro, N., Husker, A., Kostoglodov, V., Romanenko, A. & Campillo, M., 2014. Using systematically characterized low-frequency earthquakes as a fault probe in Guerrero, Mexico, *J. geophys. Res.,* **119,** 7686–7700.

Frank, W., Shapiro, N., Husker, A., Kostoglodov, V. & Campillo, M., 2016. Repeating seismicity in the shallow crust modulated by transient stress perturbations, *Tectonophysics,* **687,** 105–110

Glasby, G. & Kasahara, J., 2001. Influence of tidal effects on the periodicity of earthquake activity in diverse geological settings with particular emphasis on submarine by hydrothermal systems, *Earth Sci. Rev.,* **52,** 261 –297

González-Ruiz, J. & McNally, K., 1988. Stress accumulation and release since 1882 in Ometepec, Guerrero, Mexico: implications for failure mechanisms and risk assessments of a seismic gap, *J. geophys. Res.,* **93,** 6297–6317

Graham, S. *et al.*, 2016. Slow slip history for the MEXICO subduction zone: 2005 through 2011, *Pure appl. Geophys.,* **173,** 3445 –3465.

Guha, S., 2000. *Induced Earthquakes,* Kluwer Academic Publishers, 314pp.

Gutenberg, B. & Richter, C., 1949. *Seismicity of the Earth and Associated Phenomena,* Princeton University Press.

Gutenberg, B. & Richter, C., 1954. *Seismicity of the Earth and Associated Phenomena,* 2nd edn, Princeton University Press.

Hamada, Y., Hirono, T. & Ishikawa, T., 2011. Coseismic frictional heating and fluid-rock interaction in a slip zone within a shallow accretionary prism and implications for earthquake slip behavior, *J. geophys. Res.,* **116,** B01302.

Healy, J., Rubey, W., Griggs, D. & Raleigh, C., 1968. The Denver earthquake, *Science,* **161,** 1301 –1310

Helmstetter, A. & Sornette, D., 2003. Bath's law derived from the Gutenberg–Richter law and from aftershock properties, *Geophys. Res. Lett.,* **30,** doi:10.1029/2003GL018186.

Henderson, J. & Maillot, B., 1997. The influence of fluid flow in fault zones on patterns of seismicity: a numerical investigation, *J. geophys. Res.,* **102,** 2915 –2924

Hill, D., 1977. A model for earthquake swarms, *J. geophys. Res.,* **82,** 1347–1352.

Hill, D. & Prejean, S., 2007. Dynamic triggering, in *Treatise on Geophysics,* Vol. 4, pp. 257 –292, ed. Schubert, G., Earthquake Seismology, H. Kanamori (Series Editor), Elsevier.

Houston, H., 2015. Low friction and fault weakening revealed by rising sensitivity of tremor to tidal stress, *Nat. Geosci.,* **8,** 409 –416

Hubbert, M. & Rubey, W., 1959. Mechanics of fluid-filled porous solids and its application to overthrust faulting, *Bull. geol. Soc. Am.,* **70,** 115 –166

Husker, A., Kostoglodov, V., Cruz-Atienza, V., Legrand, D., Shapiro, N., Payero, J., Campillo, M. & Huesca- Pérez, E., 2012. Temporal variations of non-volcanic tremor (NVT) locations in the Mexican subduction zone: finding the NVT sweet spot, *Geochem. Geophys. Geosyst.,* **13,** Q03011, doi:10.1029/2011GC003916.

Husker, A., Ferrari, L., Arango-Galván, C., Corbo-Camargo, F. & Arzate-Flores, J., 2018. A geologic recipe for transient slip within the seismogenic zone: insight from the Guerrero seismic gap, Mexico, *Geology,* **46,** 35–38.

Ide, S. & Tanaka, Y., 2014. Controls on plate motion by oscillating tidal stress: evidence from deep tremors in western Japan, *Geophys. Res. Lett.,* **41,** 3842–3850

Ide, S., Yabe, S. & Tanaka, Y., 2016. Earthquake potential revealed by tidal influence on earthquake size-frequency statistics, *Nat. Geosci.,* doi:10.1038/NGEO2796.

Ishikawa, T. *et al.*, 2008. Coseismic fluid–rock interactions at high temperatures in the Chelungpu fault, *Nat. Geosci.,* **1,** 679–683.

Jödicke, H., Jording, A., Ferrari, L., Arzate, J., Mezger, K. & Rüpke, L., 2006. Fluid release from the subducted Cocos plate and partial melting of the crust deduced from magnetotelluric studies in southern Mexico: implications for the generation of volcanism and subduction dynamics, *J. geophys. Res.,* **111,** B08102, doi:10.1029/2005JB003739.

Kanjorski, N., 2003. Cocos plate structure along the middle America subduction zone off Oaxaca and Guerrero, Mexico: influence of subducting plate morphology on tectonics and seismicity, *PhD thesis*, University of California, San Diego.

Katayama, I., Terada, T., Okazaki, K. & Tanikawa, W., 2012. Episodic tremor and slow slip potentially linked to permeability contrasts at the Moho, *Nat. Geosci.,* **5,** 731–734.

Kim, Y., Clayton, R. & Jackson, J., 2010. Geometry and seismic properties of the subducting Cocos plate in central Mexico, *J. geophys. Res.,* **115,** B06310, doi:10.1029/2009JB006942.

Klein, F., 1976. Earthquake swarms and the semidiurnal solid earth tide, *Geophys. J. R. astr. Soc.,* **45,** 245–295.

Klitgord, K. & Mammerickx, J., 1982. East Pacific rise: magnetic anomaly and bathymetric framework, *Geophys. Res.,* **87,** 6725 –6750.

Kodaira, S., Iidaka, T., Kato, A., Park, J., Iwasaki, T. & Kaneda, Y., 2004. High pore fluid pressure may cause silent slip in the Nankai Trough, *Science,* **304,** 1295 –1298.

Kostoglodov, V. & Ponce, L., 1994. Relationship between subduction and seismicity in the Mexican part of the Middle America trench, *J. geophys. Res.* , **99,** 729 –742.

Kostoglodov, V., Bandy, W., Domínguez, J. & Mena, M., 1996. Gravity and seismicity over the Guerrero seismic gap, Mexico, *Geophys. Res. Lett.,* **23,** 3385 –3388.

Kostoglodov, V., Husker, A., Shapiro, N., Payero, J., Campillo, M., Cotte, N. & Clayton, R., 2010. The 2006 slow slip event and nonvolcanic tremor in the Mexican subduction zone, *Geophys. Res. Lett.,* **37,** L24301.

Kundu, B. *et al.*, 2012. The 2005 volcano-tectonic swarm in the Andaman Sea: triggered by the 2004 great Sumatra–Andaman earthquake, *Tectonics,* **31,** TC5009, doi:10.1029/2012TC003138.

Lay, T. & Wallace, T., 1995. *Modern Global Seismology,* 521pp., Academic.

Lee, W., Bennet, R. & Meaghu, K., 1972. A method of estimating magnitude of local earthquakes from signal duration, U.S. Geological Survey Open File Report, 28pp.

Legrand, D., Villagómez, D., Yepes, H. & Calahorrano, A., 2004. Multifractal dimension and *b*-value analysis of the 1998–1999 Quito swarm related to Guagua Pichincha volcano activity, Ecuador, *J. geophys. Res.,* **109,** 1–9

Legrand, D., Barrientos, S., Bataille, K., Cembrano, J. & Pavez, A., 2011. The fluid-driven tectonic swarm of Aysen Fjord, Chile (2007) associated with two earthquakes ($M_w = 6.1$ and $M_w = 6.2$) within the Liquiñe-Ofqui Fault Zone, *Cont. Shelf Res.,* **31,** 154 –161

Legrand, D., Tassara, A. & Morales, D., 2012. Megathrust asperities and clusters of slab dehydration identified by spatiotemporal characterization of seismicity below the Andean margin, *Geophys. J. Int.,* **191,** 923 –931

Legrand, D. *et al.*, 2015. Comparision of the seismicity before and after the 1982 El Chichon eruption, in *Active Volcanoes of Chiapas (Mexico): El Chichón and Tacaná, Active Volcanoes of the World,* eds Scolamacchia, T. & Macías, J.L., chap. 5, Springer, doi:10.1007/978-3-642-25890-9-5.

Liu, Y. & Rice, J., 2007. Spontaneous and triggered aseismic deformation transients in a subduction fault model, *J. geophys. Res.*: Solid Earth., **112,** doi:10.1029/2007JB004930.

Lockner, D. & Beeler, N., 1999. Premonitory slip and tidal triggering of earthquakes, *J. geophys. Res.,* **104,** 20 133–20 151

Ma, K., Brodsky, E., Mori, J., Ji, C., Song, T. & Kanamori, H., 2003. Evidence for fault lubrication during the 1999 Chi-Chi, Taiwan, earthquake (M_w7.6), *Geophys. Res. Lett.,* **30,** 1–4.

Manea, M. & Manea, V., 2011. Curie point depth estimates and correlation with subduction in Mexico, *Pure appl. Geophys.,* **168,** 1489 –1499

Matsumura, S., Ohkubo, T. & Imoto, M., 1991. Seismic swarm activity in and around the Izu Peninsula preceding the volcanic eruption of July 13, 1989, *J. Phys. Earth,* **39,** 93–106.

Maury, J., Ide, S., Cruz-Atienza, V., Kostoglodov, V., Gonzáles-Molina, G. & Péres-Campos, X., 2016. Comparative study of tectonic tremor locations: characterization of slow earthquakes in Guerrero, Mexico, *J. geophys. Res.,* **121,** 5136 –5151.

Maury, J., Ide, S., Cruz-Atienza, V. & Kostoglodov, V., 2018. Spatiotemporal variations in slow earthquakes along the Mexican subduction zone, *J. geophys. Res.,* **123**. 1559 –1575.

McNally, K. & Minster, J., 1981. Nonuniform seismics liprate along Middle America trench, *Geophys. Res.,* **86,** 4949 –4959.

McNutt, S., 1986. Observations and analysis of B-type earthquakes, explosions, and volcanic tremor at Pavlof Volcano, Alaska, *Bull. seism. Soc. Am.,* **76,** 153 –175.

McNutt, S. & Beavan, R., 1981. Volcanic earthquakes at Pavlof volcano correlated with the solid earth tide, *Nature,* **294,** 615 –618.

Métivier, L., de Viron, O., Conrad, C., Renault, S., Diament, M. & Patau, G., 2009. Evidence of earthquake triggering by the solid earth tides, *Earth Planet. Sci. Lett,* **278,** 370 –375.

Mogi, K., 1962. Magnitude–frequency relation for elastic shocks accompanying fractures of various materials and some related problems in earthquakes, *Bull. Earthq. Res. Inst. Univ. Tokyo,* **40,** 831 –853.

Montgomery-Brown, E., Segall, P. & Miklius, A., 2009. Kilauea slow slip events: identification, source inversions, and relation to seismicity, *J. geophys. Res.,* **114,** B00A03, doi:10.1029/2008JB006074.

Moore, G. & Shipley, T., 1988. Mechanisms of sediment accretion in the Middle America Trench off Mexico, *J. geophys. Res.,* **93,** 8911 –8927.

Murru, M., Montuori, C., Wyss, M. & Privitera, E., 1999. The location of magma chambers at Mt. Etna, Italy, mapped by *b*-values, *Geophys. Res. Lett.,* **26,** 2553 –2556.

Nakata, R., Suda, N. & Tsuruoka, H., 2008. Non-volcanic tremor resulting from the combined effect of Earth tides and slow slip events, *Nat. Geosci.,* **1,** 676–678.

Neunhöfer, H. & Hemmann, A., 2005. Earthquake swarms in the Vogtland/Western Bohemia region: spatial distribution and magnitude–frequency distribution as an indication of the genesis of swarms?, *J. Geodyn.,* **39,** 361–385.

Pardo, M. & Suárez, G., 1995. Shape of the subducted Rivera and Cocos plates in southern Mexico: seismic and tectonic implications, *J. geophys. Res.,* **100,** 12 357–12 373.

Payero, J., Kostoglodov, V., Shapiro, N., Mikumo, T., Iglesias, A., Péres-Campos, X. & Clayton, R., 2008. Nonvolcanic tremor observed in the Mexican subduction zone, *Geophys. Res. Lett.,* **35,** doi:10.1029/2007GL032877.

Peacock, S., Christensen, N., Bostock, M. & Audet, P., 2011. High pore pressures and porosity at 35 km depth in the Cascadia subduction zone, *Geology,* **39,** 471–474.

Pearson, C., 1981. The relationship between microseismicity and high pore pressures during hydraulic stimulation experiments in low permeability granitic rocks, *J. geophys. Res.,* **86,** 7855 –7864.

Peng, Y. & Rubin, A., 2017. Intermittent tremor migrations beneath Guerrero, Mexico, and implications for fault healing within the slow slip zone, *Geophys. Res. Lett.,* **44,** 760 –770.

Pinares, P., 2006. Study of spatial and temporal distribution of seismicity in North Chile, *Civil Engineer thesis* (in Spanish), University of Chile, Santiago, 101pp.

Pine, R. & Batchelor, A., 1984. Downward migration of shearing in jointed rock during hydraulic injections, *Int. J. Rock Mech. Min. Sci.,* **21,** 249–263.

Radiguet, M., Cotton, F., Vergnolle, M., Campillo, M., Walpersdorf, A., Cotte, N. & Kostoglodov, V., 2012. Slow slip events and strain accumulation in the Guerrero gap, Mexico, *J. geophys. Res.,* **117,** B04305, doi:10.1029/2011JB008801.

Reches, Z. & Lockner, D., 2010. Fault weakening and earthquake instability by powder lubrication, *Nature,* **467,** 452–455.

Rubinstein, J., La Rocca, M., Vidale, J., Creager, K. & Wech, A., 2008. Tidal modulation of nonvolcanic tremor, *Science,* **319,** 186 –189.

Ryall, A., VanWormer, J. & Jones, A., 1968. Triggering of microearthquakes by earth tides, and other features of the Truckee, California, earthquake sequence of September, 1966, *Bull. seism. Soc. Am.,* **58,** 215 –248.

Scholz, C., 1968. The frequency–magnitude relation of microfracturing in rock and its relation to earthquakes, *Bull. seism. Soc. Am.,* **58,** 399 –415.

Segall, P., Rubin, A., Bradley, A. & Rice, J., 2010. Dilatant strengthening as a mechanism for slow slip events, *J. geophys. Res.,* **115,** B12305.

Shelly, D., Beroza, G., Ide, S. & Nakamula, S., 2006. Low-frequency earthquakes in Shikoku, Japan, and their relationship to episodic tremor and slip, *Nature,* **442,** 188 –191.

Singh, S. & Mortera, F., 1991. Source-time functions of large Mexican subduction earthquakes, morphology of the Benioff zone and the extent of the Guerrero gap, *J. geophys. Res.,* **96,** 21 487 –21 502.

Singh, S. & Suárez, G., 1988. Regional variation in the number of aftershocks ($m_b \geq 5$) of large subduction-zone earthquakes ($M_w \geq 7.0$), *Bull. seism. Soc. Am.,* **78,** 230 –242.

Singh, S., Pérez-Campos, X., Iglesias, A. & Pacheco, J., 2008. An exploratory study for rapid estimation of critical source parameters of great subduction-zone earthquakes in Mexico, *Geofis. Int.,* **47,** 355 –369.

Skoumal, R., Brudzinski, M. & Currie, B., 2016. An efficient repeating signal detector to investigate earthquake swarms, *J. geophys. Res.,* **121,** 5880–5897.

Song, T., Helmberger, D., Brudzinski, M., Clayton, R., Davis, P., Pérez-Campos, X. & Singh, S., 2009. Subducting slab ultra-slow velocity layer coincident with silent earthquakes in southern Mexico, *Science,* **324,** 502–506.

Sottili, G., Martino, S., Palladino, D., Paciello, A. & Bozzano, F., 2007. Effects of tidal stresses on volcanic activity at Mount Etna, Italy, *Geophys. Res. Lett.,* **34,** l01311, doi:10.1029/2006GL028190.

Spada, M., Tormann, T., Wiemer, S. & Enescu, B., 2013. Generic dependence of the frequency-size distribution of earthquakes on depth and its relation to the strength profile of the crust, *Geophys. Res. Lett.,* **40,** 709 –714.

Sparks, R., 1981. Triggering of volcanic eruptions by Earth tides, *Nature,* **290,** 448, doi:10.1038/290448a0.

Suárez, G. & Albini, P., 2009. Evidence for great tsunamigenic earthquakesb (M 8.6) along the Mexican subduction zone, *Bull. seism. Soc. Am.,* **99,** 892 –896

Tanaka, S., 2010. Tidal triggering of earthquakes precursory to the recent Sumatra megathrust earthquakes of 26 December 2004 (M_w 9.0), 28 March 2005 (M_w 8.6), and 12 September 2007 (M_w 8.5), *Geophys. Res. Lett.,* **37,** L02301.

Tanaka, S., 2012. Tidal triggering of earthquakes prior to the 2011 Tohoku-Oki earthquake (M_w 9.1), *Geophys. Res. Lett.,* **39,** L00G26.

Tanaka, S., Ohtake, M. & Sato, H., 2002. Spatio-temporal variation of the tidal triggering effect on earthquake occurrence associated with the 1982 South Tonga earthquake of M_w 7.5, *Geophys. Res. Lett.,* **29,** 1756, doi:10.1029/2002GL015386.

Tanaka, S., Ohtake, M. & Sato, H., 2004. Tidal triggering of earthquakes in Japan related to the regional tectonic stress, *Earth Planets Space,* **56,** 511–515.

Thomas, A., Nadeau, R. & Bürgmann, R., 2009. Tremor-tide correlations and near-lithostatic pore pressure on the deep San Andreas fault, *Nature,* **462,** 1048 –1051.

Thomas, A., Bürgmann, R., Shelly, D., Beeler, N. & Rudolph, M., 2012. Tidal triggering of low frequency earthquakes near Parkfield, California: implications for fault mechanics within the brittle-ductile transition, *J. geophys. Res.,* **117,** B05301.

Tolstoy, M., Vernon, F., Orcutt, J. & Wyatt, F., 2002. Breathing of the seafloor: tidal correlations of seismcity at Axial volcano, *Geology,* **30,** 503 –506.

Tsuruoka, H., Ohtake, M. & Sato, H., 1995. Statistical test of the tidal triggering of earthquakes: contribution of the ocean tide loading effect, *Geophys. J. Int.,* **122,** 183–194.

UNAM Seismology Group, 2013. Ometepec-Pinotepa Nacional, Mexico earthquake of 20 March 2012 (M_w 7.5): a preliminary report, *Geofis. Int.,* **52**(2), 173–196.

Van Camp, M. & Vauterin, P., 2005. Tsoft: graphical and interactive software for the analysis of time series and Earth tides, *Comput. Geosci.,* **31**(5), 631–640.

Villafuerte, C. & Cruz-Atienza, V., 2017. Insights into the causal relationship between slow slip and Tectonic Tremor in Guerrero, Mexico, *J. geophys. Res.,* **122,** 6642 –6656.

Vorobieva, I., Shebalin, P. & Narteau, C., 2016. Break of slope in earthquake size distribution and creep rate along the San Andreas Fault system, *Geophys. Res. Lett.,* **43,** 6869 –6875.

Waldhauser, F., Schaff, D., Diehl, T. & Engdahl, E., 2012. Splay faults imaged by fluid-driven aftershocks of the 2004 M_w 9.2 Sumatra–Andaman earthquake, *Geol. Soc. Am.,* **40,** 243–246.

Wang, J.H., 1988. *b* values of shallow earthquakes in Taiwan, *Bull. seism. Soc. Am.,* **78,** 1243 –1254.

Wiemer, S. & Benoit, J., 1996. Mapping the *b*-value anomaly at 100 km depth in the Alaska and New Zealand subduction zones, *Geophys. Res. Lett.,* **23,** 1557–1560.

Wiemer, S. & McNutt, S., 1997. Variations in frequency–magnitude distribution with depth in two volcanic areas: Mount St. Helen, Washington, and Mount Spurr, Alaska, *Geophys. Res. Lett.,* **24,** 189–192.

Wyss, M., 1973. Towards a physical understanding of the earthquake frequency distribution, *Geophys. J. R. astr. Soc.,* **31,** 341 –3 59.

Wyss, M., Klein, F., Nagamine, K. & Wiemer, S.& 2001. Anomalously high *b*-values in the South Flank of Kilauea volcano, Hawaii: evidence for the distribution of magma below Kilauea's East rift zone, *J. Volc. Geotherm. Res.,* **106,** 23 –37.

Yabe, S., Tanaka, Y., Houston, H. & Ide, S., 2015. Tidal sensitivity of tectonic tremors in Nankai and Cascadia subduction zones, *J. geophys. Res.,* **120,** 7587–7605.

Yamamoto, J., Quintanar, L. & Jimenez, Z., 2002. Why earthquake doublets in the Ometepec, Guerrero, Mexico subduction area?, *Phys. Earth planet. Inter.,* **132,** 131 –139.

Yamamoto, J., GonzálezMoran, T., Quintanar, L., Zavaleta, A., Zamora, A. & Espindola, V.H., 2013. Seismic pattern of the Guerrero-Oaxaca, Mexico region, and its relationship to the continental margin structure, *Geophys. J. Int.,* **192,** 375 –389.

Yoon, C., O'Reilly, O., Bergen, K. & Beroza, G., 2015. Earthquake detection through computationally efficient similarity search, *Sci. Adv.,* **1,** e1501057, doi:10.1126/sciadv.1501057.

Yoon, C., Huang, Y., Ellsworth, W. & Beroza, G., 2017. Seismicity during the initial stages of the Guy-Greenbrier, Arkansas, earthquake sequence, *J. geophys. Res.,* **122,** doi:10.1002/2017JB014946.

SUPPORTING INFORMATION

Supplementary data are available at *GJI* online.

Figure S1. Original raw data in the north, east and vertical directions (thin curve) and in the *P*, *SV* and *SH* rotated directions (bold curve) (top). It is clear that the wave comes from the SW. Polarization ellipsoid in the horizontal and vertical plans during the first 0.5 s after the *P*-wave arrival time (bottom).

Figure S2. The generalized Wadati method of double difference of *P* and *S* traveltimes for 8753 earthquake-station pairs. The slope gives V_p/V_s directly (see Annex A for details). The size and colour of each point are proportional to the number of readings.

Figure S3. Difference of longitudes and latitudes between the locations corresponding to the 50 events located with the single station PNIG and the seven local broad-band seismometers.

Figure S4. Daily average noise variations for 31 d (January 2012, blue lines) calculated on 15 min time windows, in a frequency band of 2–20 Hz, in a 24 H circular diagram. The average of the daily noise of the blue lines of the 31 d is plotted as the red curve. Time is local time.

Table S1: The characteristics of the main-shock hypocentre are given by using different methods and seismic agencies. Backazimuth and distance are with respect to station PNIG.

Table S2. Length × width (km × km) and area (km^2) of the main shock using different methods. For comparison, the size of the 1982 earthquake determined by formula $M_w = \log_{10}(A) + 4$ (Singh *et al.* 2008) and distribution of all aftershocks are 1445 and 2450 km^2, respectively.

Please note: Oxford University Press is not responsible for the content or functionality of any supporting materials supplied by the authors. Any queries (other than missing material) should be directed to the corresponding author for the paper.